Automation in Construction 109 (2020) 102965

Contents lists available at ScienceDirect

Automation in Construction

journal homepage: www.elsevier.com/locate/autcon

Multi-scale roof characterization from LiDAR data and aerial orthoimagery: Automatic computation of building photovoltaic capacity

J. Martín-Jiménez*, S. Del Pozo, M. Sánchez-Aparicio, S. Lagüela

Department of Cartographic and Land Engineering, University of Salamanca, Hornos Caleros, 50, Ávila 05003, Spain

ARTICLE INFO

Keywords:
Geometric characterization
Roofs
Photovoltaic energy
LiDAR
Orthoimagery
Solar potential
Automation

ABSTRACT

Photovoltaic self-consumption in buildings requires the installation of photovoltaic (PV) systems mostly on roofs, taking the advantage of these building locations for both the available surface area and the certainty of a big amount of annual incoming solar radiation. Since the parameters required for a proper PV system design are mainly geometric: azimuth-orientation, tilt angle and effective dimensions of the different roof slopes; aerial LiDAR data and orthoimagery offered by the National Geographic Agencies became suitable data sources for this purpose, ensuring its availability for any city regardless of its location. This paper presents a novel automatic methodology that combines LiDAR and orthoimage data processing to geometrically characterize roofs at slope level and calculate their PV solar potential. The methodology developed has been validated against results obtained from a higher-resolution aerial 3D point cloud of the roofs under study. Different locations and roof types have been tested in order to confirm the performance of the methodology under different conditions, being able to accurately characterize the geometry of most types of roofs, such as flat roofs, gable or saddle roofs, single pitched roofs and pyramid roofs at city, neighbourhood and building level.

1. Introduction

The use of solar energy has been a subject of increasing interest in the last years, supplying the 6.6% of the total primary energy production of renewable energy in Europe in 2017 [1] and with a great increase regarding the contribution of 2% to the total energy production in 2007. In addition, the growing concern about the climate change issue has led to a rising willingness of consumers to become self-consumers, also encouraged by national governments in an attempt to increase their share in renewable energy consumption [2].

Within this framework, and thanks to the reduction of investment costs of photovoltaic (PV) panels due to the maturity of this technology [3], PV solar energy constitutes an option of interest for the building users, especially for its exploitation in their main places of consumption (home and work). In a commitment towards the distributed energy generation and self-consumption to avoid energy losses due to transportation, the ideal place for installing PV systems is in the buildings themselves. Specifically, roofs are chosen as the main location for the PV installation due to their favourable position with respect to the Sun [4]. That is, roofs ensure the minimum energy-loss and optimize installation costs, as well as maximize the reception of Sun radiation. For this reason, the location, characteristics and dimensions of roofs are critical when analysing the feasibility, production and profitability of PV installations [5]. In this regard, there are tools available to estimate the PV energy production of roofs, such as Google SunRoof [6]. While this kind of tools allows the analysis of costs and profitability of PV installations on roofs, they have limitations derived from: (i) the use of two-dimensional data, (ii) ideal values of solar production and (iii) disregarding the real yields of the panels.

With the aim at avoiding the 2D limitation, LiDAR data and photogrammetry have arisen as providers of the information about the third dimension, allowing the simultaneous computation of the roof parameters for several buildings [7–11]. However, most of the existing approaches come from commercial software [7] or calculate the solar potential of roofs without discretizing between the different roof slopes and their different azimuth-orientations and tilt angles [8]. Other approaches make use of aerial imagery for 3D building reconstruction, in such way that the accuracy commonly associated to the spatial resolution of this imagery is lost in the generation of the Digital Surface Model [9]. Provided the complexity and variety of existing roofs, some works [12] present a methodology focusing on pitched-roofs. However, this approach is object-oriented, and computes the solar energy potential for individual buildings. While this is a valid approach in regions with single family houses, it cannot be applied in urban areas where the

* Corresponding author.
E-mail addresses: joseabula@usal.es (J. Martín-Jiménez), s.p.aguilera@usal.es (S. Del Pozo), mar_sanchez1410@usal.es (M. Sánchez-Aparicio), sulaguela@usal.es (S. Lagüela).

https://doi.org/10.1016/j.autcon.2019.102965
Received 5 April 2019; Received in revised form 10 September 2019; Accepted 11 September 2019
Available online 24 October 2019

Table 1
Comparison between the methodology proposed and the state of the art.

Existing works	Reference	Strengths of the proposed methodology compared to existing works
Arefi & Reinartz, 2013	[16]	Automatic computation of roof parameters, not limited to the geometric modelling but including data exploitation.
Fan et al., 2014	[17]	More robust and more accurate results due to the combination of two data sources (LiDAR and aerial orthoimagery) instead of being dependent on the resolution and precision of a single data source (LiDAR data).
Ghaffarian & Ghaffarian, 2014	[18]	Buildings are not only detected but parametrized, providing characterization data useful for further purposes such as for PV potential computation.
Martín et al., 2015	[8]	Lower computation requirements thanks to the processing at roof level.
Wang et al., 2015	[19]	Symmetric and asymmetric roof structures can be analysed.
Ghaffarian & Ghaffarian, 2016	[20]	Extraction of roof parameters useful for further purposes such as PV potential computation: azimuth-orientation, tilt angle and dimensions of each roof slope.
Kiti et al., 2017	[14]	The methodology does not rely on third-party software for any step, including the computation of solar radiation.
Li and Liu, 2017	[12]	The 3D modelling regarding the extraction of parameters of interest (azimuth-orientation, tilt angle and dimensions of each roof slope) is fully automatic.
Palmer et al., 2018	[7]	Self-developed methodology not relying on third-party software. No manual procedures are required.
Zhao et al., 2018	[21]	Alternative methodology with which not only extract roofs but also obtain their azimuth-orientation, tilt angle and effective dimensions.
Pirotti et al., 2019	[22]	Façades are automatically discarded on the first steps of the algorithm. Roofs are detected and modelled with the parameters required for the determination of solar radiation.

solar radiation of buildings is affected by the radiation of their surroundings [13]. In this sense, [14] computed roof solar potential based on LiDAR data and for complete neighbourhoods, taking into account how the buildings of the surroundings affect in terms of projected shadows. However, the use of LiDAR data alone presents limitations in terms of occlusions, spatial resolution and horizontal accuracy that can be solved by its combination with aerial imagery [15]. A summary of the contribution of the methodology proposed regarding the state of the art is presented in Table 1.

Accordingly, the proposed methodology allows an accurate estimation of solar production in roofs based on their 3D characterization in terms of location, azimuth-orientation, morphology and dimensions for most existing roof types (Fig. 1). This is possible due to the optimization of each data source for their combined processing in order to compute such geometric parameters. While LiDAR data is used for the computation of the angular parameters of the roofs, aerial orthoimagery provides accurate information about the contours of the roofs due to its high spatial resolution. The main contribution of this paper is the full automation of the roof characterization, discriminating between the different roof slopes per building, and processing several buildings simultaneously (going from city to roof scale). In this way, it is possible to perform studies at city, neighbourhood or building level obtaining high precision results with a great level of detail for all cases.

In order to describe the proposed methodology, the paper is organized as follows. After this introduction, both the data sources and the workflow of the methodology proposed are described in detail in Section 2. The evaluation system and experimental results at city, neighbourhood and building level are firstly described in Section 3 and then discussed in Section 4. Finally, the conclusions and future works are summarized in Section 5.

2. Data sources

Given that the main purpose of this research work is to present a standard methodology for the decision-making regarding PV installations in roofs, the focus is set on the use of available free geomatic data that guarantees precision in the results. The methodology makes use of LiDAR data and aerial orthoimagery in a combined way (Fig. 2) to automatically obtain the location, azimuth-orientation, tilt angle and dimensions of each of the slopes of the roof analysed. These are the main parameters required to perform an appropriate query to any solar radiation database in order to obtain PV potential of the roof. In addition, the importance of an accurate estimation of these parameters when performing feasibility and profitability studies of PV installations on roofs should be highlighted.

2.1. Data description

As already mentioned, the methodology developed uses two data sources as input: i) 3D point clouds from aerial LiDAR technology and ii) aerial orthoimagery, both widely used and available data sources in most countries (especially in Europe, through the INSPIRE standard [23]). In this case, both data sources are in the same reference system (ETRS89) and are available at the download centre of the Spanish National Geographic Agency [24]. This national agency analyses changes in the Spanish territory based on aerial data acquired every 2 or 3 years.

While, at first instance LiDAR technology seemed to be ideal and enough to perform 3D geometric analysis, it is limited by its spatial resolution, horizontal accuracy and the concavity/convexity in some building boundaries [15,25]. Since one of the key parameters when calculating PV solar potential is the total available area, the detection of

Fig. 1. Typology of roofs solved satisfactorily with this novel methodology: single pitched roofs (a), flat roofs (b), gable or saddle roofs (c and d) and pyramid roofs (e). Source of the images: Google Maps ©.

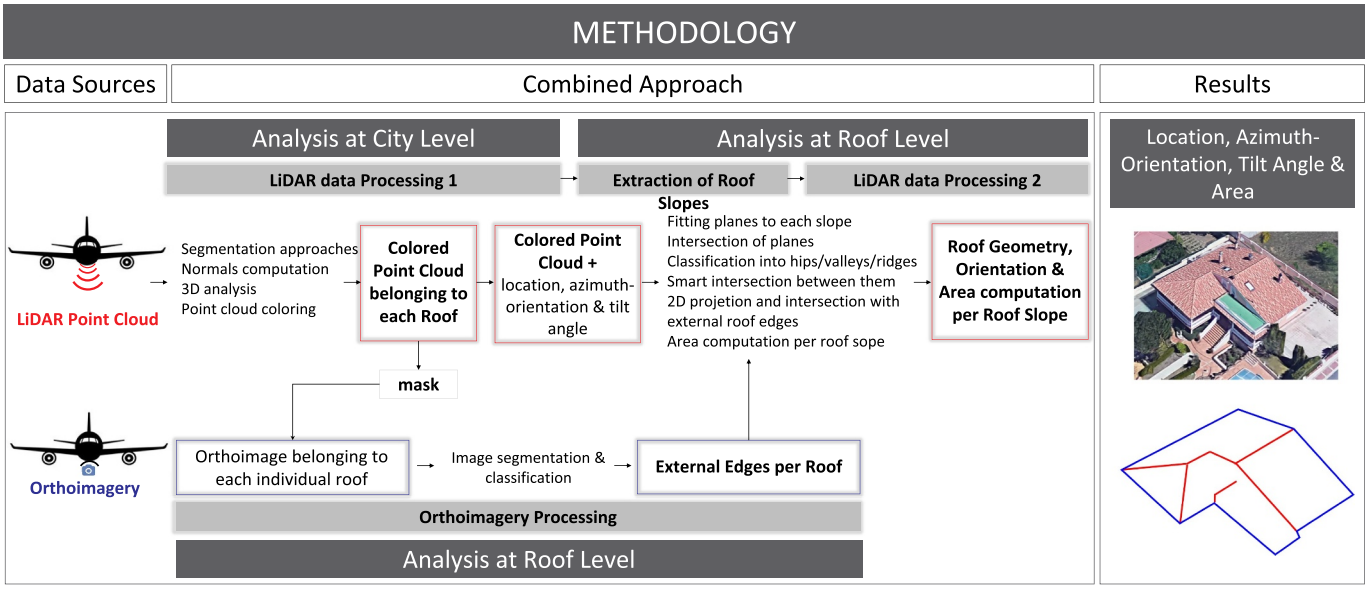

Fig. 2. Workflow of the methodology proposed for the 3D characterization of roofs in order to assess their PV potential.

Table 2
Main features of the input data used by the proposed methodology.

Data source		
Aerial LiDAR data	Accuracy	± 20 cm (Z), ± 40 cm (XY)
	Spatial resolution	0.5–1 p/m^2
	Geodesic reference	ETRS89
	Wavelength	1064 nm (infrared)
	Coverage	4 km^2
	Information stored in the point cloud	XYZ coordinates, RGB data, point source id, user data, scan angle, flight line edge, scan direction, returns, return number, GPS time, classification and infrared intensity
	Type of LiDAR	Optech ALTM 3025 (time-of-flight)
	Format	LAZ 1.1
Aerial orthoimages	Accuracy	± 50 cm
	Spatial resolution	25 cm
	Geodesic reference	ETRS89
	Type of camera	Vexcel UltraCam (large format aerial digital camera)
	Format	ECW

exterior roof edges is required when evaluating solar potential at roof level. In this sense, LiDAR data is limited and should be hybridized with another data source that allows boundaries detection with guarantees of accuracy, such as aerial orthoimagery (Table 2).

Therefore, in the proposed methodology, aerial LiDAR data is used to: (i) segment the roofs from the whole LiDAR point cloud, (ii) extract their location, (iii) detect the number of slopes per roof, (iv) calculate their azimuth-orientation and (v) tilt angle per roof slope, (vi) define the roof structure (ridge, rips and valleys) and (vii) serve as a mask for the identification of roofs in the orthoimagery processing. Then, orthoimagery is applied to determine the exterior roof edges which serve to delimit the area belonging to each specific roof slope. In this way, both technologies offer their advantages and their combination ensures accuracy in terms of planimetric, altimetric and angular characterization.

2.2. Aerial LiDAR data

This data source offers ranging accuracy for 3D documentation, characterization and reconstruction, especially in terms of altimetry (Table 2). However, it is crucial to analyse its limitations in terms of spatial resolution to discern which elements could be properly characterized and which could not. The aerial LiDAR data used in this study is available in .LAZ files at the IGN data repository [24]. This cartographic data has very low spatial resolution, specifically, between 0.5 and 1 points per square meter depending on the flight strip overlap. Therefore, even though it is a high precision 3D data source, it is inadvisable to use it for calculating roof dimensions since it would result in their underestimation.

2.3. Aerial orthoimagery

The aerial orthoimages from the Spanish National Orthophotography Program (PNOA, Spanish acronym) [24] are the result of a photogrammetric network captured by a large format digital camera (Vexcel UltraCam). A longitudinal overlap between images of 60% and a transversal overlap ≥25% was considered for this photogrammetric network. As a result, an orthoimage with a GSD of 25 cm (Table 2) is obtained, resulting in a great advantage in terms of spatial resolution. This resolution allows one to obtain an accurate estimation of the roof's external edges by means of digital image procedures such as edge detector algorithms and segmentation procedures. Despite its high spatial resolution, this bidimensional product is not useful to define the angular roof parameters on its own, i.e. azimuth-orientation, tilt angle and real area of each roof slope. Regarding its planimetric accuracy, this cartographic product offers a precision of ± 50 cm.

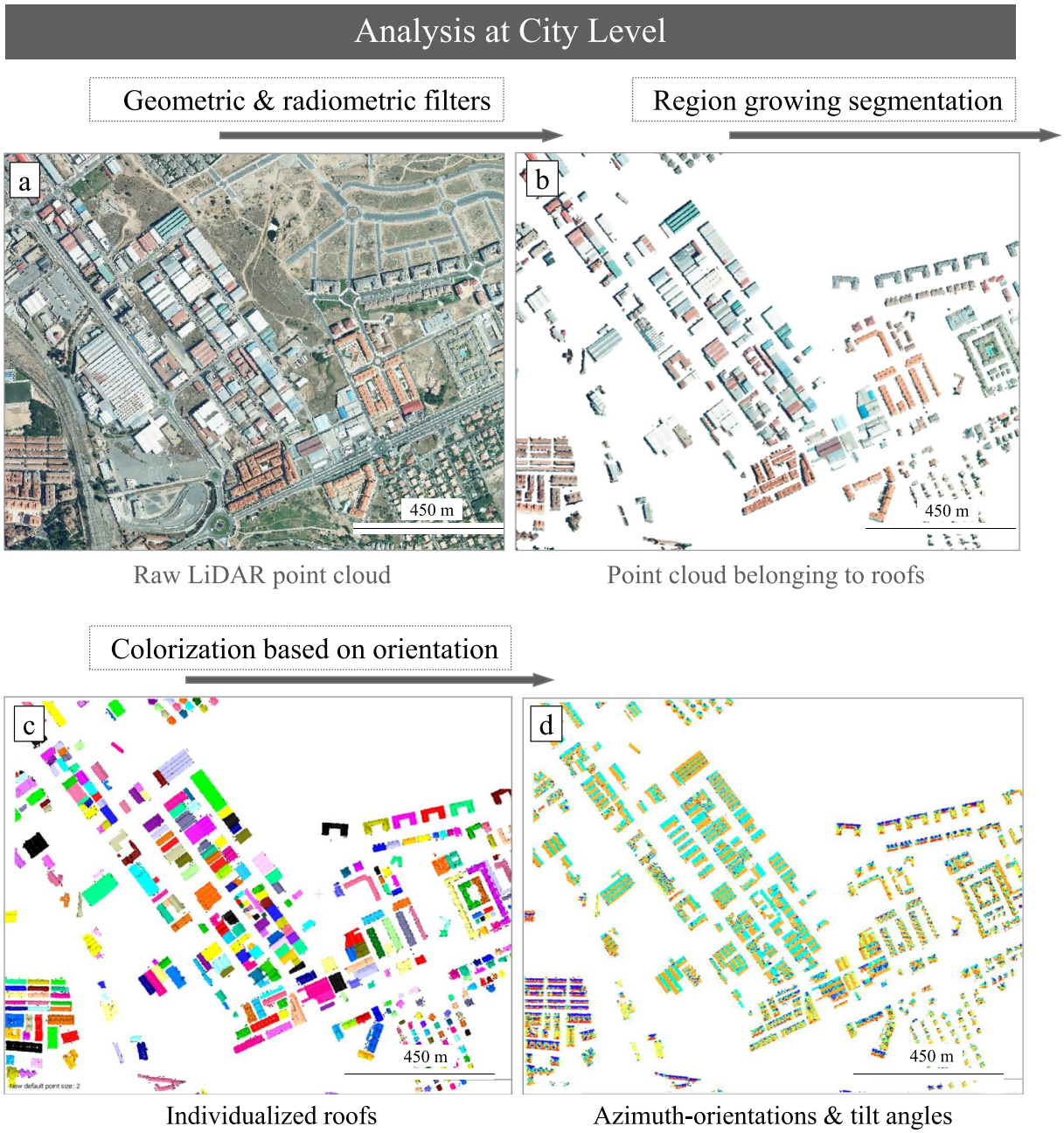

Fig. 3. LiDAR data processing at city level. (For interpretation of the references to colour in this figure, the reader is referred to the web version of this article.)

3. Methodology

As shown in the workflow diagram (Fig. 2), the procedure begins with the LiDAR data processing, from which the layer corresponding to individualized roofs with information about their location, azimuth-orientation and tilt angle is obtained. Then, the point cloud corresponding to each individual roof serves as a mask and input data to the orthoimagery processing where it is used to crop the matching orthoimage regarding the buildings under study. After the appropriate image processing (Section 2.3), the exterior roof edges are obtained. Finally, these edges serve as external delimitation to accurately quantify the area of each roof slope identified through the LiDAR processing. Below, all the phases and algorithms implemented in the proposed methodology are described in detail.

3.1. LiDAR data processing (LDP)

This approach integrates several steps and two correlative working scales: one at city level (CL) (Fig. 3) and the other at individual roof level (RL) (Fig. 6). To operate at individual RL, the proposed methodology integrates a sequential segmentation procedure based on both geometric and radiometric criteria. All the algorithms and methods implemented are described below in their order of application.

3.1.1. LDP at city level: location, azimuth-orientation and tilt angle

The result is the point cloud corresponding only to roof areas coloured according to the azimuth-orientation (Fig. 4b) and with information regarding both roof azimuth-orientation and tilt angle after going through the following 8 steps:

- CL1-Removal of points belonging to the ground. Only those points

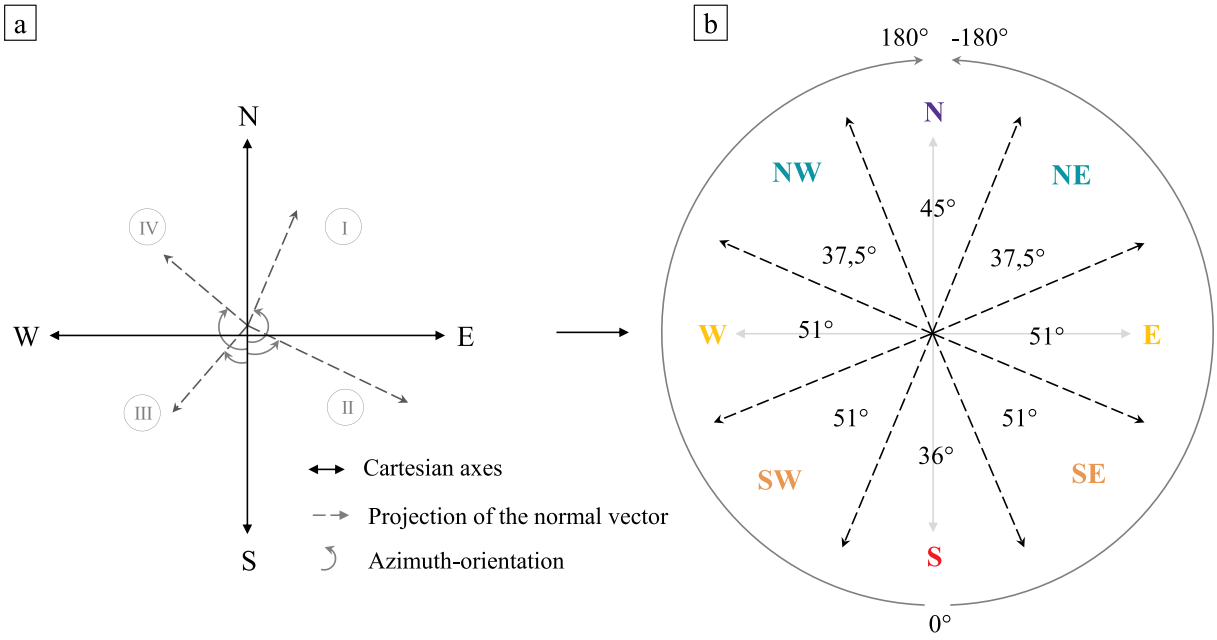

Fig. 4. (a) The four quadrants in which the Cartesian axes are divided as well as the projection of the normal vector on them. (b) The colour assigned to each point according to the 8 orientations established in the Spanish Technical Building Code (CTE [30]). (For interpretation of the references to colour in this figure legend, the reader is referred to the web version of this article.)

with a single LiDAR return (Table 2) continue in the process, in order to ensure that they correspond to solid surfaces (Fig. 3a–b).

- CL2-Removal of points belonging to vegetation areas. A previous computation of the Normalized Vegetation Index (NDVI) [26] is required (Fig. 3a–b). It is quantified thanks to the red and near infrared information collected by the LiDAR (Table 1) and by applying Eq. (1).

$$NDVI = \frac{NIR - RED}{NIR + RED},\ where\ (-1 < NDVI < 1) \quad (1)$$

A NDVI threshold of 0.3 [26,27] was established in such a way that points with higher NDVI value are considered vegetation and consequently removed.

- CL3-Removal of points belonging to building façades. This segmentation is based on the Z-component of the normal vector (**Nz**) of each 3D point. Each normal vector is estimated through the adjustment of a 2D subspace that is tangent at the point of interest based on pairwise point relationships [28]. Specifically, a surface is adjusted to the 8 nearest neighbour points of each 3D point analysed (search resolved by k-d tree) within a maximum radius of 4 m. In this calculation, the covariance matrix of the 8 points is analysed and the normal vector of the surface adjusted is determined as the normal vector of the analysed point. A threshold of 0.15 was established in such a way that any point with a **Nz** value below this threshold is considered a point corresponding to façades due to the verticality of the surface adjusted.
- CL4-Removal of remaining noise points. Possible residual points from the previous steps are deleted by applying a Statistical Outlier Removal (SOR) filter [29]. A threshold of 1-m deviation in 30 neighbour points was established. After this step, the resulting point cloud corresponds only to roof areas (Fig. 3b).
- CL5-Individualization of roofs. Each roof is individualized by means of a region growing segmentation establishing a cluster size of 20 cm in the 20 nearby neighbours (Fig. 3c).
- CL6-Azimuth-orientation computation. The azimuth-orientation and tilt angle of the roofs are calculated by analysing the X-Y-Z-components of the normal vector (**Nx**, **Ny** and **Nz**) of each point (Fig. 3c–d). This requires projecting the normal vector to the horizontal plane and evaluating its corresponding quadrant (Fig. 4a). The azimuth-orientation ($-180^\circ < Azi < 0 < Azi < 180^\circ$) is calculated by Eqs. (2), (3) and (4), depending on the normal vector, so if it belongs to the 1st, 2nd and 3rd, or to the 4th quadrant respectively (Fig. 4).

$$Azi\,(^\circ) = \tan^{-1}\frac{Nx}{Ny} - 180 \quad (1^{st}\ \text{quadrant}) \quad (2)$$

$$Azi\,(^\circ) = \tan^{-1}\frac{Nx}{Ny} \quad (2^{nd}\ \text{and}\ 3^{rd}\ \text{quadrant}) \quad (3)$$

$$Azi\,(^\circ) = 180 + \tan^{-1}\frac{Nx}{Ny} \quad (4^{th}\ \text{quadrant}) \quad (4)$$

- CL7-Point cloud colorization. Once the azimuth-orientation is computed, the point cloud belonging to roofs is coloured (Fig. 3d) following the criteria of Fig. 4b.
- CL8-Tilt angle computation. This is the last step of the LiDAR data processing at CL. It is calculated by a simple trigonometric process outlined in Fig. 5 and Eq. (5).

$$Tilt\,(^\circ) = 90 - \left[\tan^{-1}\left(\frac{\boldsymbol{Nz}}{\sqrt[2]{\boldsymbol{Nx}^2 + \boldsymbol{Ny}^2}}\right)\right] \quad (5)$$

3.1.2. LDP at roof level: internal roof edges and dimensions of roof slopes

In order to calculate the azimuth-orientation, tilt angle and dimensions of each roof slope it is necessary to determine the number of roof slopes per building under study. However, before starting this analysis, each roof has to be classified as flat or non-flat. Specifically, a threshold of 0.5% is established to highlight the difference between the vertical and the horizontal component, in such a way that if the difference (in absolute value) between the mean values of the **Nz** and **Nx** and between the mean values of the **Nz** and **Ny** is < 0.5% the roof is classified as flat roof. It should be noted that these roofs are characterized by a point cloud with mixed colours in reference to the azimuth-orientation colorization (Fig. 11-2d). In such cases, the azimuth-orientation is established as "flat", the tilt angle is the mean/average

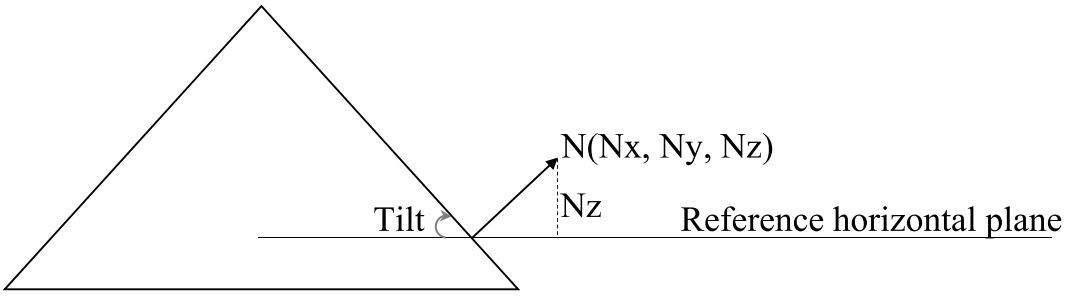

Fig. 5. Tilt angle of a roof slope based on the analysis of the normal vector.

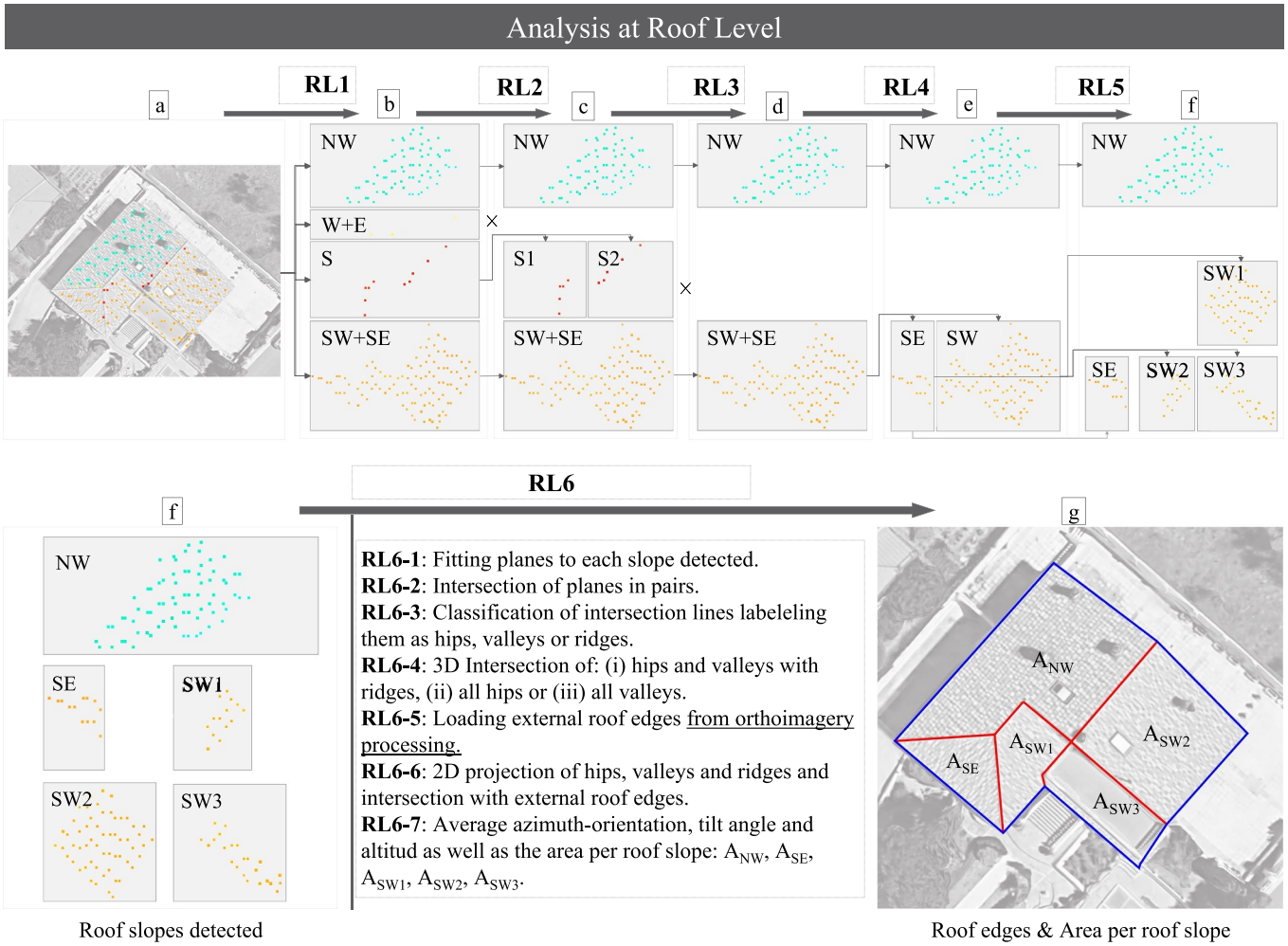

Fig. 6. Workflow of the LiDAR data processing at roof level for non-flat roofs. (For interpretation of the references to colour in this figure, the reader is referred to the web version of this article.)

value of all points of the roof and the area is obtained with the external roof edges from the orthoimagery processing.

For non-flat roofs, the number of roof slopes and their main geometric parameters are obtained after applying the following 6 steps outlined in Fig. 6, where each colour indicates a different orientation of the roof (step CL7):

- RL1-Colour Segmentation. Taking as basis the colours assigned to each point in the step CL7, the point cloud of each roof is segmented into as many groups as colours.
- RL2-Region growing segmentation. Each of the point groups after RL1 is segmented based on region growing establishing a cluster size of 10 cm in the 10 nearby neighbours. Some groups of points disappear because they are considered noise due to their low point density. This is the case of the yellow points (West and East facing) in Fig. 6.
- RL3-Spatial dispersion filter. At this step, spatially dispersed groups of points are removed, even if they have a good point density. The criterion to consider spatial dispersion was the ratio between the variance (in both X and Y dimensions) and the number of points. A threshold of 1.3 was established in such a way that groups of points with higher dispersion value, are removed, given that it is highly probable that those points do not belong to any roof slope. They should belong to roof edges due to the change of curvature in those areas. This is the case of red points (South facing) in Fig. 6.
- RL4-Positive/Negative azimuth segmentation. Those groups of

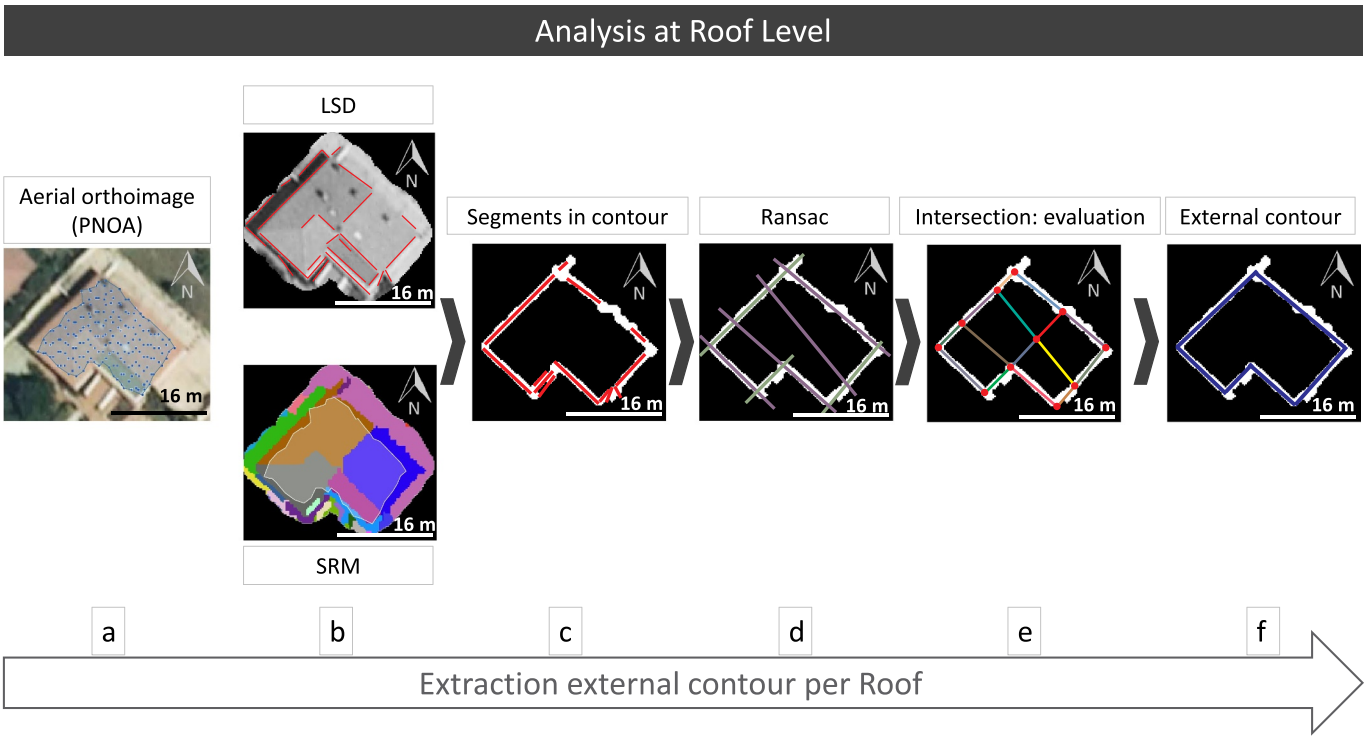

Fig. 7. Methodological workflow to get the external edges of each roof.

points that have passed the RL1, RL2 and RL3 segmentations are divided into groups of points with positive and negative azimuth in case of having both. This is the case of orange points in Fig. 6 (South-East and South-West facing).

- RL5-Inclination dispersion filter. In this step, the tilt angle value of all the points belonging to each group is analysed in terms of dispersion. If a high change of tilt angle is computed, the group is divided into as many subgroups as tilt angles are computed. This is the case of the South-West orange group in Fig. 6, which was divided into 3 different groups (SW1, SW2 and SW3) belonging to 3 different roof slopes.
- RL6-Roof edge parametrization. This is the final step of the LiDAR processing where each point group, representative of each roof slope, is subjected to 7 sequential steps after which the internal roof edges are parametrized. Thanks to the detection of these boundaries and those coming from the orthoimagery processing (Section 2.3) it is possible to accurately estimate the dimensions of each roof slope as well as the average value of the corresponding azimuth-orientation and tilt angle:

  RL6-1. Fitting planes to each of the 3D point groups throughout the M-estimator Sample and Consensus (MSAC) algorithm [31]. The maximum distance threshold established for a point to be considered by the MSAC algorithm is 0.4 m, compatible with the planimetric precision of LiDAR data (Table 2).

  RL6-2. Intersection of planes in pairs based on a neighbourhood criterion. Given the low resolution offered by the LiDAR data used in this study and the loss of points through the previous processing steps, an average distance adaptive threshold of 8 m (adaptation regarding the size of the building) is established to determine the neighbourhood between roof slopes.

  RL6-3. Classification of the intersection lines into (i) ridges, (ii) valleys and/or (iii) hips depending on their slope in Z axis. If the slope is < 2% it is considered as a ridge. The remaining lines are classified as valleys if the 3D points of the surroundings have higher Z-coordinate and as hips if they have lower Z-coordinate.

  RL6-4. In case there are the three types of lines, lines classified as valleys and/or hips are 3D intersected with those classified as ridges, and in case there are only valleys or hips, they are intersected in pairs.

  RL6-5. In this step, the orthoimagery processing is linked to the LiDAR processing through the incorporation of the outer edges defined in the orthoimagery process (in blue). These external boundaries will serve as outer limits to the 2D intersection of ridges, hips and valleys in order to define precisely each roof slope.

  RL6-6. The 2D projection of ridges, hips and valleys and the intersection with outer limits is performed. At this point, each roof slope is accurately defined.

  RL6-7. Finally, the area of each roof slope defined is computed, in 2D firstly and in 3D later thanks to the tilt angle value.

3.2. Orthoimagery processing: external roof edges and total roof area

The orthoimagery processing for the external roof edges detection and the computation of the total roof area consists on a triple-stage procedure (Fig. 7).

3.2.1. Roof mask

A combined processing between the individual roofs (RL) from the LiDAR procedure and the orthoimagery is carried out to go from the CL to the RL in the orthoimagery. The result of this combination allows one to know the area of the orthoimage in which the roof is located. Making a mask from the contour of the point cloud corresponding to each individual roof, a positive 2 m buffer is created so that the roof and its immediate surroundings fit within. This process is required given the low spatial resolution of the LiDAR data and in order to solve the overestimation of the external boundaries of roofs by using this data source. As a result, an image mask is obtained, and the following stages are performed per roof (Fig. 7a).

3.2.2. Boundaries detection strategies

In order to define the external roofs edges from the orthoimage, a

Fig. 8. Perspective view of part of the city of Ávila. (a) Raw LiDAR point cloud with true RGB values. (b) Incorporation of the roof layer in red. (c) Roof layer colourized according to the azimuth-orientation of roofs and with information about their tilt angles. (For interpretation of the references to colour in this figure legend, the reader is referred to the web version of this article.)

procedure consisting on the parallel application of an image segmentation and an identification of straight contours is applied (Fig. 7b). Image segmentation is performed using the Statistical Region Merging (SRM) algorithm [32], which is based on region growing and merging techniques. The identification of straight contours on the orthoimagery is performed with the Line Segment Detector (LSD) algorithm [33,34]. This algorithm detects lines based on the image gradient orientation of each pixel, so that lines are composed of adjacent pixels with the same image gradient orientation, which is different from the image gradient orientation of the surrounding pixels.

The image segmentation is applied to detect those pixels strictly corresponding to roof and non-roof areas. Pixels corresponding with roof areas are put together and the contour of the final "roof group" is determined.

The LSD is applied as a double validation of the pixels corresponding to the external roof edges. Since the LSD algorithm results in the extraction of lines from the exterior contour of the roof but also from the interior of the roof (i.e. lines that define the different roof slopes), the double validation by the SRM algorithm allows the strict definition of the external roof edges (Fig. 7c).

In the case that more than one line-segment are detected for one external roof edge, RANSAC algorithm [35] is applied to combine them in one line (Fig. 7d).

3.2.3. External edges detection

Lines from Stage 2 are intersected (Fig. 7e) with the aim at obtaining the real external contour of the roof (Fig. 7f). The contour obtained after the application of the SRM algorithm is used as reference, especially for the case of irregular roofs (for example, U-shaped). In the case the intersection point between lines is within the reference contour, it is considered as a real intersection point. If there are more than one intersection points in the same edge, the most external ones are considered as the real boundaries of the roof.

4. Results

This section deals with the application of the proposed methodology to several buildings and case studies in order to check its scalability and suitability to accurately characterize roofs at city, neighbourhood and building level of those countries with geospatial data within the INSPIRE standards. The case studies were a sample of buildings in the city of Ávila (Spain) and in the city of Vaihingen an der Enz (Germany). Specifically, the data of the city of Ávila corresponded to:

- Free aerial data offered by the Spanish National Geographic Agency at the IGN data repository [24] that was used geometrically

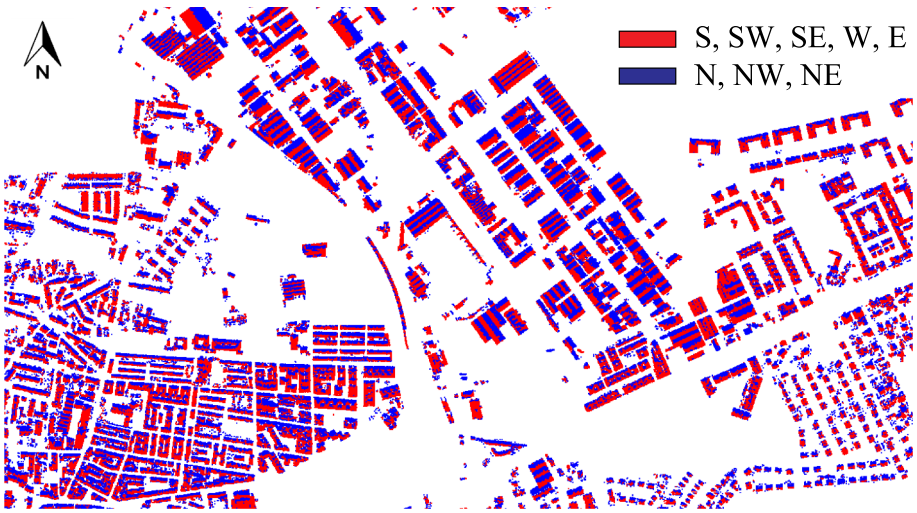

Fig. 9. Plan view of part of the roofs of the city of Ávila where the favourable orientations for the installation of PV systems have been coloured in red (S, SW, SE, W and E) and those unfavourable in blue (N, NW and NE). (For interpretation of the references to colour in this figure legend, the reader is referred to the web version of this article.)

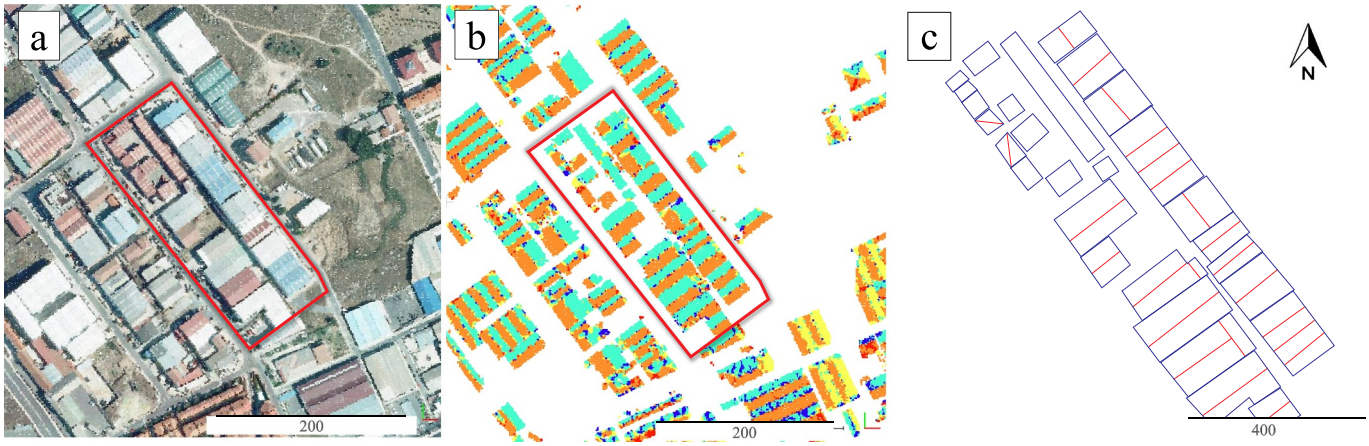

Fig. 10. Roof characterization of the chosen neighbourhood (red polygon) in the industrial estate of Ávila. Plan view of: (a) the raw LiDAR point cloud, (b) processed point cloud corresponding to roofs coloured according to the azimuth-orientation and with tilt angle information, and (c) the final vector result with information about the azimuth-orientation, tilt angle and area per roof slope. (For interpretation of the references to colour in this figure legend, the reader is referred to the web version of this article.)

Table 3
Roof characterization parameters obtained for the 28 buildings analysed at neighbourhood scale in the city of Ávila.

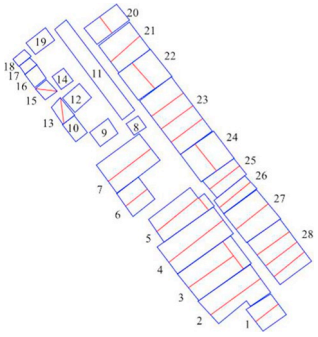

characterize roofs at city, neighbourhood and building level.
- A higher resolution aerial data commissioned by the City Council of Ávila that was used to compare both results.

Regarding the data of the city of Vaihingen an der Enz it corresponded to:

- Aerial data offered by the German Society of Photogrammetry, Remote Sensing and Geoinformation (DGPF).
- Reference data available within the framework of an ISPRS test project [36] that served as ground truth to validate the proposed methodology for the automatic characterization of roofs.

4.1. Roof characterization at city level

For this purpose, six LiDAR data sheets of the city of Ávila from the IGN data repository were used covering 24 km^2. Fig. 8 shows the results obtained after applying the proposed methodology to this aerial LiDAR data (Table 2).

It can be concluded that roofs of the city of Ávila have a predominant Northeast orientation with 18.75%. Other orientations are distributed as follows: 13.07% of roof slopes oriented to the North, 13.04% to the Southeast, 12.75% to the Southwest, 10.86% to the West, 10.61% to the South, 10.60% to the East and 10.32% to the Northwest (Fig. 8c). On the other hand, it can be figured that the average tilt angle of the roof slopes of the city is 21.61°.

Facing the installation of solar panels on roofs, arguably 57.86% of the roofs of Ávila have a favourable orientation for the direct installation of integrated PV panels, without changing their orientation on the roof (Fig. 9). This percentage corresponds to the roof slopes oriented to the South, Southwest, Southeast, West and East.

4.2. Roof characterization at neighbourhood level

To test the methodology at neighbourhood level, a set of 28 buildings from the industrial estate of Ávila (Fig. 10), located at the Northeast of the city, was selected. This area was chosen because most of the roofs of industrial buildings have any of the typologies (Fig. 1) for which the automatic characterization has been resolved through the proposed methodology.

Then, in Table 3, all the parameters obtained after applying the methodology proposed in the chosen study area are summarized.

Under the assumption of a perfect symmetry of the roof slopes of the buildings 1, 4, 6, 7, 13, 15, 20, 21, 22, 23, 24, 25, 26, 27 and 28, which were identified as symmetrical through the analysis of the orthoimages, a RMSE of ± 5.25% is derived from the area estimation per roof slope when using low resolution LiDAR data (0.5 p/m^2, Table 2). For the case study and given that the average area per roof slope for those buildings supposed symmetrical was 313.63 m^2, the area of each roof slope has been overestimated or underestimated by an average of 16.47 m^2.

4.3. Roof characterization at building level

For this analysis 4 buildings of the city of Ávila were chosen based on their roof typology: a single pitched roof, a flat roof, a slope gable roof and a pyramid roof were analysed (Fig. 11). Results obtained after applying the proposed methodology are summarized in Table 4.

5. Validation and discussion

In order to validate the methodology, two analysis have been performed in different cities and datasets features. For the city of Ávila, the validation consisted in comparing results obtained for the 28 industrial buildings of Fig. 10 when processing the free available aerial data offered by the Spanish National Geographic Agency and when processing a 4 times higher spatial resolution aerial data. The latest corresponds to a 2 points per square meter LiDAR point cloud from a flight commissioned by the City Council of Ávila in 2010. For the city of Vaihingen an der Enz, the validation involved the comparison of the results obtained after processing orthoimagery and LiDAR data provided by the DGPF with the reference values offered by the ISPRS test project [36]. In this case, the residential area called “Area 3” was chosen and the spatial

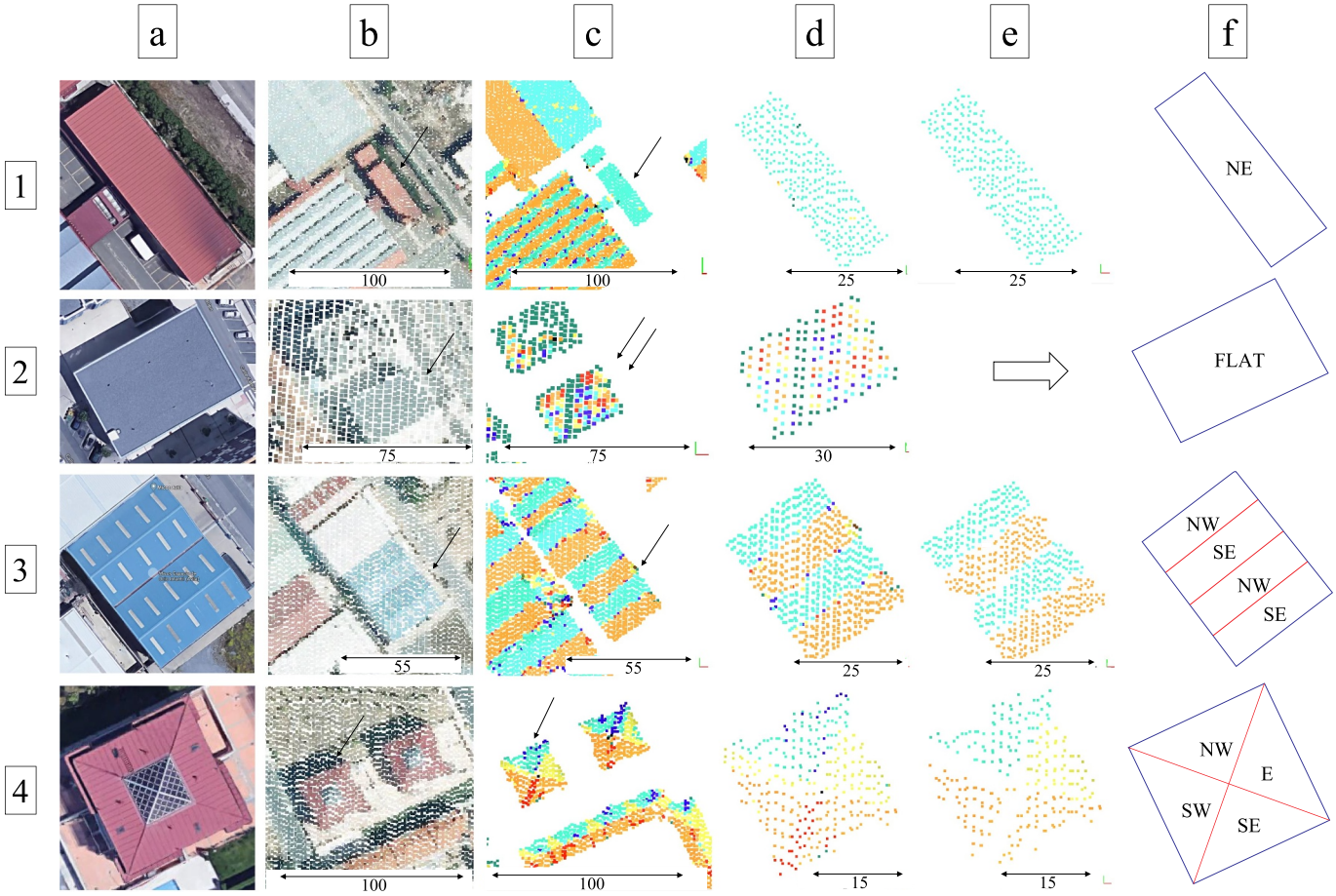

Fig. 11. Roof characterization of the four chosen buildings of the city of Ávila. (a) Plan view of: a (1) single pitched roof, a (2) flat roof, a (3) 4-slope gable roof and a (4) pyramid roof; source: Google Maps ©. Being (b) the raw LiDAR point cloud, (c) the processed point cloud corresponding to roofs coloured according to the azimuth-orientation and information regarding tilt angles after applying the CL8 step of the methodology, (d) the individual roof of interest, (e) points belonging to each roof slope detected after applying the step RL5, note that in case of flat roofs, the processing finishes in "d" when they are identified as flat roofs (see Section 3.1.2); and (f) the final vector result obtained after applying the step RL6 of the methodology that contains information regarding the azimuth-orientation, tilt angle and area per roof slope.

Table 4
Roof characterization parameters obtained for the 4 buildings analysed at building scale.

Building	Roof slope	Azimuth (0°–360°)	Orientation	Tilt angle (°)	Area (m^2)	Altitude (m)
1	1	52.96°	NE	10.13°	483.89	1141.50
2	1	FLAT	FLAT	FLAT	769.07	1151.80
3	1	322.28°	NW	10.92°	309.17	1149.60
	2	143.57°	SE	10.16°	323.96	1149.60
	3	323.19°	NW	10.24°	263.95	1149.60
	4	142.44°	SE	10.70°	224.31	1149.60
4	1	334.34°	NW	18.34°	136.71	1177.20
	2	65.65°	E	18.14°	129.77	1177.10
	3	153.65°	SE	17.72°	134.97	1177.00
	4	243.98°	SW	17.87°	135.99	1177.10

resolution of data was 8 cm for the orthoimages and 4 points per square meter for the LiDAR data.

5.1. Validation for the data set of Ávila (Spain)

The azimuth-orientation, tilt angle, area and altitude of the 28 buildings analysed in Section 3.2 are here updated (Table 5) with results obtained after applying the methodology to the higher spatial resolution LiDAR data of the same area (Fig. 12).

As in Section 3.2, under the assumption of perfect symmetry between the roof slopes of buildings 1, 4, 6, 7, 13, 15, 20, 21, 22, 23, 24, 25, 26, 27 and 28, a RMSE of 2.63% is derived from the area estimation per roof slope for this case study when using a 2 p/m^2 point cloud LiDAR data, and given that the average area per roof slope for those groups of symmetrical buildings was 313.63 m^2.

By comparing results obtained from both LiDAR data sets (Table 6) the following is concluded:

- Angular parameters (azimuth-orientation and tilt angle) presented an average error below 1°: 0.19% and 0.45% respectively considering 360° and 90° for azimuth-orientation and tilt angle, which are below the adjustment accuracies offered by solar panel supports [37].
- The altitude estimation highlighted for its low error, 0.02 m in this case study. This is due the precision offered by LiDAR technology in altimetry measurements (around 20 cm, Table 2).
- Area per roof slope obtained an average error of 14.51 m^2 which corresponds to an error in percentage of 4.63% taking as reference the average area of the roof slopes analysed (313.63 m^2). It would suppose an underestimation or overestimation of 7 panels (of 2 m^2) in roofs with capacity for 156 panels. For residential use, where 10 panels are usually installed per roof, this would lead to underestimating or overestimating the installation in 1 or zero panels (0.45 panels of 2 m^2).

Table 5
Roof characterization parameters obtained for the 28 buildings analysed at neighbourhood scale when using the 2 p/m^2 LiDAR data.

Building	Roof slope	Azimuth (0°–360°)	Orientation	Tilt angle (°)	Area (m^2)	Altitude (m)
1	1	142.36°	SE	10.88°	203.67	1143.60
	2	322.44°	NW	11.14°	203.12	1143.60
2	1	143.77°	SE	6.20°	515.02	1148.00
	2	322.33°	NW	6.39°	511.56	1147.80
3	1	142.04°	SE	15.31°	493.70	1147.40
	2	321.84°	NW	15.42°	497.78	1147.20
	3	FLAT	FLAT	3.14°	250.85	1142.60
4	1	144.08°	SE	5.67°	620.65	1145.70
	2	322.24°	NW	5.65°	610.34	1145.70
5	1	144.26°	SE	4.74°	420.00	1147.40
	2	323.24°	NW	4.68°	408.04	1147.40
	3	325.44°	NW	3.46°	42.21	1143.50
6	1	143.38°	SE	16.43°	197.30	1148.00
	2	323.62°	NW	15.77°	216.01	1147.60
7	1	143.00°	SE	5.55°	494.37	1149.30
	2	322.76°	NW	5.52°	494.41	1149.20
8	1	55.77°	NE	11.29°	106.12	1150.30
9	1	143.19°	SE	8.86°	217.17	1150.40
10	1	227.49°	SW	10.48°	167.46	1150.50
11	1	52.17°	NE	11.11°	831.74	1150.50
12	1	320.98°	NW	9.16°	203.65	1150.30
13	1	270.95°	W	7.78°	67.53	1152.10
	2	92.32°	E	5.76°	69.46	1152.10
14		143.22°	SE	10.24°	118.18	1150.30
15	1	8.27°	N	9.39°	56.84	1152.40
	2	187.91°	S	8.39°	60.51	1152.10
16	1	233.62°	SW	10.57°	128.25	1150.30
17	1	233.17°	SW	11.44°	78.60	1150.30
18	1	322.83°	NW	9.84°	68.74	1147.60
19	1	321.49°	NW	11.19°	217.87	1150.30
20	1	231.77°	SW	5.85°	221.26	1153.90
	2	53.27°	NE	5.85°	220.04	1153.80
21	1	322.91°	NW	5.61°	373.08	1155.70
	2	143.44°	SE	5.60°	330.11	1153.70
22	1	232.97°	SW	5.66°	365.70	1155.70
	2	52.70°	NE	5.65°	369.01	1155.70
23	1	323.32°	NW	5.48°	378.1	1153.30
	2	143.08°	SE	5.45°	296.6	1153.10
	3	323.36°	NW	5.54°	356.82	1153.20
	4	142.88°	SE	5.53°	299.56	1153.30
24	1	232.64°	SW	5.60°	375.49	1153.80
	2	53.24°	NE	5.63°	367.25	1153.70
25	1	324.11°	NW	12.46°	205.86	1151.80
	2	143.91°	SE	10.81°	207.69	1151.70
26	1	323.81°	NW	11.98°	221.96	1152.10
	2	142.95°	SE	8.48°	224.61	1152.40
27	1	323.15°	NW	3.34°	399.59	1153.60
	2	143.39°	SE	3.42°	405.06	1153.50
28	1	322.51°	NW	10.21°	292.48	1149.60
	2	143.43°	SE	10.35°	274.65	1149.60
	3	322.56°	NW	10.35°	288.46	1149.60
	4	142.91°	SE	10.77°	265.80	1149.60

- Assuming perfect symmetry between the roof slopes of the buildings 1,4, 6, 7, 13, 15, 20, 21, 22, 23, 24, 25, 26, 27 and 28, the improvement on the results of area calculation using the higher spatial resolution LiDAR data validates the methodology, since the error is dependent on the data source.

5.2. Validation for the data set of Vaihingen an der Enz (Germany)

Finally, in order to validate the performance of the proposed methodology with ground-truth reference data, a sample of buildings from a residential neighbourhood of the city of Vaihingen an der Enz was analysed. Specifically, the neighbourhood called “Area 3” in the ISPRS test project [36] that has 47 buildings and for which reference data is available. “Area 3” was chosen from among the three areas offered because most of the roofs (42 of the 47) have a morphology that can be characterized by the proposed methodology. However, the analysis was carried out in 41 buildings since there was a scarce LiDAR data recorded for the building located to the right of the building 2 in Fig. 13. This is due to the fact that slate roofs absorb the infrared radiation [38], spectral range for which the LiDAR used by the DGPF operates (Leica ALS50).

After segmenting the point cloud by eliminating the 6 buildings that were not analysed for the aforementioned reasons, the methodology was applied for the point cloud with the 41 remaining buildings. The geometrical parameters obtained for each roof slope are summarized in Table 7.

Since the average altitude of the ground of such neighbourhood (Z coordinate of the LiDAR data) was 266.50 m and that of the roofs analysed was 273.42, it was concluded that it is a low-rise residential neighbourhood with buildings of an average height of 6.92 m ± 3.55 m.

In order to check the results obtained and validate the methodology, each geometric parameter was compared with its corresponding reference value offered by the ISPRS test project [36]. Table 8 shows the comparative analysis after which the following conclusions were derived:

- Angular parameters (azimuth-orientation and tilt angle) presented an average error around 1°, matching the results obtained in the test site of the city of Ávila. These uncertainty values are below the adjustment accuracies offered by solar panel supports [37].
- An average error of 6.97 m^2 was obtained when evaluating the area per roof slope. It corresponds to an error in percentage of 2.93% taking as reference an area of 238.29 m^2. This error supposes an underestimation or overestimation of 3 PV panels (of 2 m^2). Better results have been obtained compared to those of the city of Ávila due to the greater spatial resolution offered by the aerial data provided by the DGPF.
- The altitude estimation had a 0.10 m average error, a slightly higher error than the one obtained in the test site of the city of Ávila. However, in both cases, errors are insignificant for the solar radiation computation.

6. Conclusions

The proposed methodology effectively solves the automatic parameterization of roofs at city, neighbourhood and building level from the combined use of discrete aerial LiDAR data and aerial orthoimagery and for the vast majority of existing roof types: single pitched roofs, flat roofs, gable or saddle roofs and pyramid roofs. In addition, the possibility of processing at city level allows the performance of prospective studies, towards the analysis of possibilities and establishment of regulations and incentives by the urban and regional Administrations.

The methodology involves not only the automatic extraction of roof boundaries but also the parametrization of each roof slope in terms of azimuth-orientation, tilt angle, altitude and effective dimensions, which are the parameters required for the computation of the PV capacity of roofs. However, it should be highlighted that the methodology is sensitive to changes in the resolution of the input data, in such a way that important improvements in accuracy are obtained with higher resolution data sets. Specifically, significant improvements have been obtained regarding the delimitation of the roof slopes and the computation of their dimensions when comparing results from higher spatial resolution orthoimagery and LiDAR data. This is because a higher density point cloud provides a better definition of the elements and therefore, in the case of the building roofs, allows a better differentiation of each roof slope and a better fit of planes. As for the rest of the parameters, very precise results are obtained in the angular measurements for both higher and lower spatial resolution aerial data. Specifically, an average error of 0.20% was obtained in the azimuth-orientation estimation, 1.29% in the tilt angle estimation, 0.63% in the

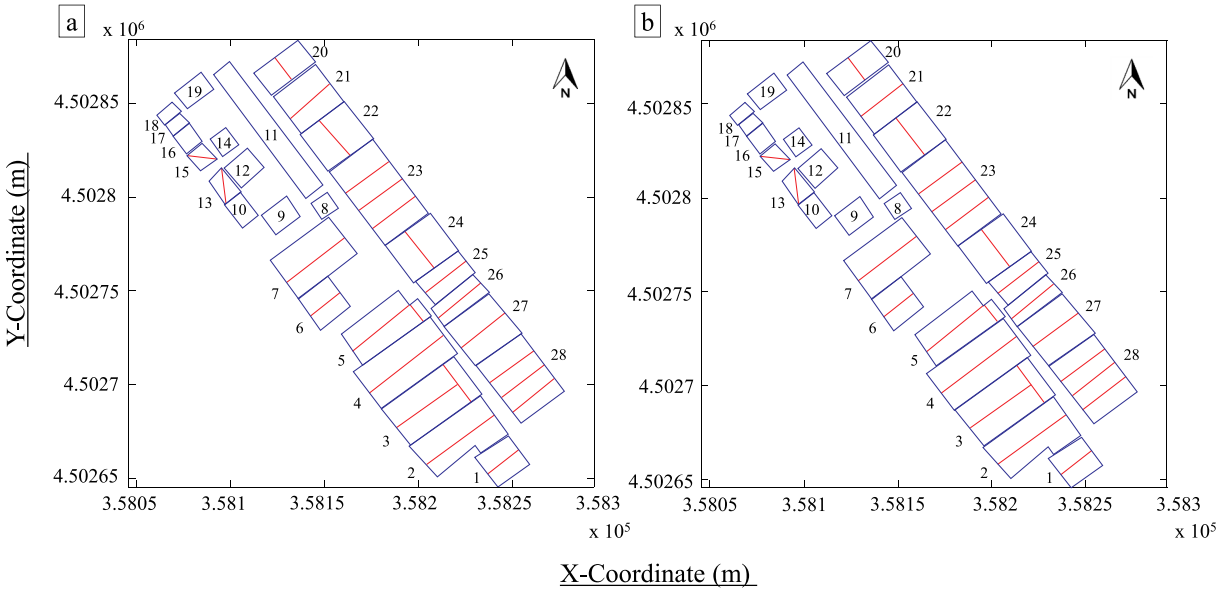

Fig. 12. Roof characterization parameters obtained for the 28 buildings analysed at neighbourhood scale when using (a) the LiDAR data of 0.5 p/m^2 resolution and when using (b) the LiDAR data of 2 p/m^2 resolution. The abscissa and ordinate represent the X and Y coordinates respectively in EPSG 25830 projection (ETRS89/UTM zone 30N).

Table 6
Uncertainty estimation taking as real values those obtained after processing the higher spatial resolution LiDAR data set (2 p/m^2). Values in bold indicate the relative average error in percentage.

	Azimuth (°)	Tilt angle (°)	Area per roof slope (m^2)	Altitude (m)
Min error	0.01°	0.01°	0.45	0.00
Max error	4.27°	1.08°	76.83	0.10
Average error	0.70°	0.40°	14.51	0.02
Average error (%)	**0.19%**	**0.45%**	**4.63%**	**0.15%**
(Reference)	(360°)	(90°)	(313.63 m^2)	(15 m)

altitude estimation and 2.93% in the area per roof slope estimation.

Future works will present a three-fold approach: on the one hand, focusing on the improvement of the characterization of the roofs, the authors will deal with the detailed study and analysis of hipped roofs to include them in the methodology in order to make it applicable to all typologies of existing roofs. In addition, procedures to automatically detect the projected shadows on roofs will be designed based on the altitude value and making a study of the sight line of each building. Finally, the analysis of the PV potential will be performed by integrating the study of the effect of the geomorphology of the soil on the incident solar radiation to PV surfaces.

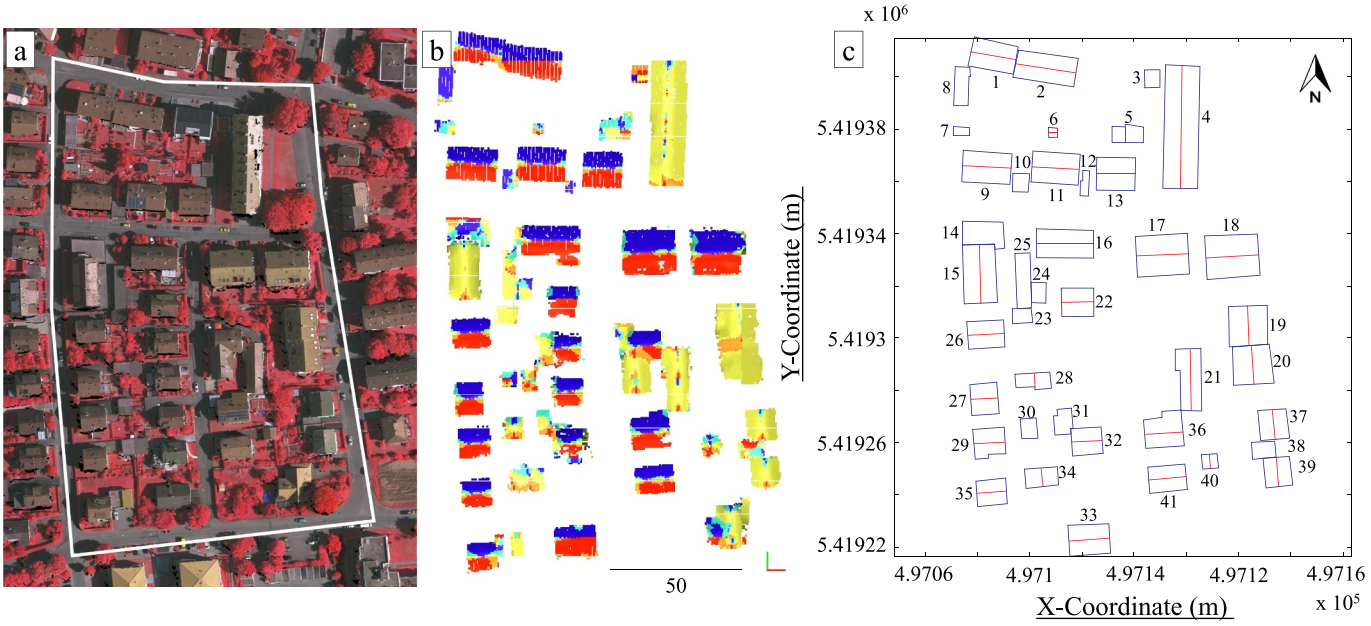

Fig. 13. Roof characterization of the chosen neighbourhood in the city of Vaihingen an der Enz. (a) Orthoimage of the neighbourhood in false colour, (b) processed point cloud corresponding to roofs coloured according to the azimuth-orientation and with tilt angle information, and (c) the final result with information about the azimuth-orientation, tilt angle and area per roof slope. Note that in (c) the abscissa and ordinate represent the X and Y coordinates respectively in EPSG 25832 projection (ETRS89/UTM zone 32N).

Table 7
Roof characterization parameters obtained for the 41 buildings analysed at neighbourhood scale when using 4 p/m^2 LiDAR data and an orthoimage resolution of 8 cm.

Building	Roof slope	Azimuth (0°–360°)	Orientation	Tilt angle (°)	Area (m^2)	Altitude (m)
1	1	10.99°	N	23.36°	100.74	270.00
	2	191.39°	S	21.29°	102.86	270.25
2	1	9.28°	N	24.60°	138.13	270.49
	2	189.05°	S	24.82°	133.98	270.55
3	1	FLAT	FLAT	1.18°	39.20	263.60
4	1	91.29°	E	26.74°	346.68	275.97
	2	271.10°	W	27.01°	352.07	275.91
5	1	FLAT	FLAT	2.01°	43.08	266.77
	2	FLAT	FLAT	1.95°	31.48	266.09
6	1	7.75°	N	7.70°	5.88	267.40
	2	188.75°	S	12.33°	6.01	267.44
7	1	FLAT	FLAT	2.96°	19.73	266.79
8	1	0.84°	N	4.55°	81.01	265.59
9	1	3.57°	N	35.47°	133.30	273.85
	2	183.59°	S	35.31°	133.85	273.75
10	1	2.33°	N	2.56°	43.22	267.99
11	1	3.49°	N	28.16°	122.61	272.89
	2	182.50°	S	27.88°	121.11	272.95
12	1	2.74°	N	2.71°	27.43	267.71
13	1	1.93°	N	31.14°	104.28	273.73
	2	180.37°	S	31.07°	109.02	273.51
14	1	FLAT	FLAT	0.92°	144.68	270.58
15	1	268.08°	W	41.45°	161.49	276.16
	2	88.15°	E	41.84°	172.91	276.07
16	1	2.32°	N	34.26°	142.21	273.50
	2	180.72°	S	33.32°	139.50	273.61
17	1	356.52°	N	32.20°	184.63	276.64
	2	176.83°	S	32.19°	182.52	276.61
18	1	356.85°	N	31.75°	186.69	276.26
	2	177.18°	S	32.30°	195.96	276.41
19	1	267.28°	W	33.16°	134.60	277.10
	2	87.12°	E	33.08°	130.76	276.84
20	1	266.67°	W	33.44°	127.24	275.36
	2	87.06°	E	33.21°	133.30	275.51
21	1	268.94°	W	30.05°	115.04	273.02
	2	88.55°	E	31.79°	124.98	273.29
22	1	355.13°	N	35.94°	77.29	273.45
	2	178.80°	S	37.07°	80.71	273.48
23	1	267.11°	W	5.14°	45.38	270.76
24	1	272.08°	W	3.87°	44.13	269.47
25	1	87.56°	E	6.04°	118.84	269.56
26	1	353.01°	N	30.51°	84.75	275.72
	2	178.20°	S	31.57°	85.69	275.53
27	1	356.04°	N	29.57°	71.07	277.49
	2	176.46°	S	28.85°	70.05	277.50
28	1	32.71°	NE	7.05°	38.01	271.59
	2	199.52°	SW	6.09°	41.31	271.48
29	1	355.44°	N	28.32°	24.26	278.62
	2	174.70°	S	29.71°	43.38	278.83
30	1	104.88°	E	23.58°	51.92	272.71
31	1	281.96°	W	5.86°	64.29	271.71
32	1	355.38°	N	45.58°	83.76	275.85
	2	175.56°	S	44.70°	74.33	276.02
33	1	355.45°	N	27.75°	103.88	275.95
	2	175.20°	S	22.63°	95.75	276.19
34	1	87.49°	E	2.94°	48.82	273.27
	2	264.89°	W	4.38°	39.39	273.21
35	1	355.22°	N	30.36°	64.29	278.70
	2	175.26°	S	29.67°	62.85	278.66
36	1	354.72°	N	34.89°	95.35	274.79
	2	175.17°	S	36.17°	72.48	275.31
37	1	265.21°	W	33.39°	75.75	275.49
	2	84.91°	E	34.76°	77.14	275.53
38	1	FLAT	FLAT	1.79°	58.15	271.42
39	1	264.66°	W	32.83°	68.12	275.74
	2	85.60°	E	33.29°	69.01	275.75
40	1	266.37°	W	21.02°	16.96	272.54
	2	86.96°	E	23.15°	16.00	272.55
41	1	354.06°	N	26.07°	80.44	277.19
	2	174.74°	S	26.57°	76.84	277.21

Table 8
Uncertainty analysis when results obtained after processing the aerial data with the proposed methodology are compared with the ground truth data offered by the ISPRS Test Project. Values in bold indicate the relative average error in percentage.

	Azimuth (°)	Tilt angle (°)	Area per roof slope (m^2)	Altitude (m)
Min error	0.02°	0.09°	0.01	0.01
Max error	4.08°	3.62°	40.59	0.17
Average error	0.71°	1.16°	6.97	0.10
Average error (%)	**0.20%**	**1.29%**	**2.93%**	**0.63%**
(Reference)	(360°)	(90°)	(238.29 m^2)	(15 m)

Declaration of competing interest

Authors declare that this work is original, the information reported in the paper is accurate according to the best knowledge of the authors, the paper has not been previously published or submitted elsewhere, and the authors are aware of ELSEVIER policy on plagiarism and self-plagiarism and there is not conflict of interest.

Acknowledgements

Authors would like to thank Iberdrola S.L. and University of Salamanca for the funding provided through Cátedra Iberdrola VIII Centenary. We also express our gratitude to the Ministry of Science, Innovation and Universities for the funding given for the project RTC-2017-6291-3.

Funding

This work was supported by the Ministry of Science, Innovation and Universities of Spain [project RTC-2017-6291-3]; and Cátedra Iberdrola-USAL VIII Centenary.

References

[1] Eurostat, Community Innovation Survey of Renewable Energy Statistics of the European Communities, Office for Official Publications of the European Communities, 2017 Available at https://ec.europa.eu/eurostat/statistics-explained (Last access: 27/03/2019).
[2] Spanish Official State Bulletin, BOE, BOE-A-2018-13593 About Urgent Measures for Energy Transition and Consumer Protection, Available at https://boe.es/eli/es/rdl/2018/10/05/15 (Last access: 27/03/2019).
[3] S. Castellanos, D.A. Sunter, D.M. Kammen, Rooftop solar photovoltaic potential in cities: how scalable are assessment approaches? Environ. Res. Lett. 12 (12) (2017) 125005, , https://doi.org/10.1088/1748-9326/aa7857.
[4] M.C. Brito, S. Freitas, S. Guimarães, C. Catita, P. Redweik, The importance of facades for the solar PV potential of a Mediterranean City using LiDAR data, Renew. Energy 111 (2017) 85–94, https://doi.org/10.1016/j.renene.2017.03.085.
[5] M. Fionnuala, K. McDonnell, A feasibility assessment of photovoltaic power systems in Ireland; a case study for the Dublin Region, Sustainability 9 (2) (2017) 302, https://doi.org/10.3390/su9020302.
[6] Google's Project Sunroof, Available at https://google.com/get/sunroof (Last access: 27/03/2019).
[7] D. Palmer, E. Koubli, I. Cole, R. Gottschalg, T. Betts, A GIS-based method for identification of wide area rooftop suitability for minimum size PV systems using LiDAR data and photogrammetry, Energies 11 (12) (2018) 3506, https://doi.org/10.3390/en11123506.
[8] A.M. Martín, J. Domínguez, J. Amador, Applying LIDAR datasets and GIS based model to evaluate solar potential over roofs: a review, AIMS Energy 3 (3) (2015) 326–343, https://doi.org/10.3934/energy.2015.3.326.
[9] S. Schuffert, T. Voegtle, N. Tate, A. Ramírez, Quality assessment of roof planes extracted from height data for solar energy systems by the EAGLE platform, Remote Sens. 7 (12) (2015) 17016–17034, https://doi.org/10.3390/rs7121586.
[10] K. Chen, W. Lu, F. Xue, P. Tang, L.H. Li, Automatic building information model reconstruction in high-density urban areas: augmenting multi-source data with architectural knowledge, Autom. Constr. 93 (2018) 22–34, https://doi.org/10.1016/j.autcon.2018.05.009.
[11] D. Li, M. Lu, Integrating geometric models, site images and GIS based on Google Earth and keyhole markup language, Autom. Constr. 89 (2018) 317–331, https://doi.org/10.1016/j.autcon.2018.02.002.
[12] Y. Li, C. Liu, Estimating solar energy potentials on pitched roofs, Energy Build. 139 (2017) 101–107, https://doi.org/10.1016/j.enbuild.2016.12.070.

[13] J. Sarralde, D.J. Quinn, D. Wiesmann, K. Steemers, Solar energy and urban morphology: scenarios for increasing the renewable energy potential of neighbourhoods in London, Renew. Energy 73 (2015) 10–17, https://doi.org/10.1016/j.renene.2014.06.028.
[14] S. Kiti, V. Wang, B. Sharp, Rooftop solar potential based on LiDAR data: bottom-up assessment at neighbourhood level, Renew. Energy 111 (2017) 463–475, https://doi.org/10.1016/j.renene.2017.04.025.
[15] T. Schenk, B. Csathó, Fusion of LIDAR data and aerial imagery for a more complete surface description, Int. Arch. Photogramm. Remote Sens. Spat. Inf. Sci. 34 (3/A) (2002) 310–317, https://doi.org/10.1109/DFUA.2003.1219962.
[16] H. Arefi, P. Reinartz, Building reconstruction using DSM and orthorectified images, Remote Sens. 5 (4) (2013) 1681–1703, https://doi.org/10.3390/rs5041681.
[17] H. Fan, W. Yao, Q. Fu, Segmentation of sloped roofs from airborne LiDAR point clouds using ridge-based hierarchical decomposition, Remote Sens. 6 (4) (2014) 3284–3301, https://doi.org/10.3390/rs6043284.
[18] S. Ghaffarian, S. Ghaffarian, Automatic building detection based on Purposive FastICA (PFICA) algorithm using monocular high-resolution Google Earth images, ISPRS J. Photogramm. Remote Sens. 97 (2014) 152–159, https://doi.org/10.1016/j.isprsjprs.2014.08.017.
[19] H. Wang, W. Zhang, Y. Chen, M. Chen, K. Yan, Semantic decomposition and reconstruction of compound buildings with symmetric roofs from LiDAR data and aerial imagery, Remote Sens. 7 (10) (2015) 13945–13974, https://doi.org/10.3390/rs71013945.
[20] S. Ghaffarian, S. Ghaffarian, Z. Samir, Y. Ruicheck, Automatic building roof segmentation based on PFICA algorithm and morphological filtering from LiDAR point clouds, 37th Asian Conference on Remote Sensing, ACRS 2016: Spatial Data Infrastructure for Sustainable Development, 2016 https://ris.utwente.nl/ws/portalfiles/portal/42925411/Ghaffarian2016automatic.pdf (Last access: 21/10/2019).
[21] R. Zhao, M. Pang, M. Wei, Accurate extraction of building roofs from airborne light detection and ranging point clouds using a coarse-to-fine approach, J. Appl. Remote. Sens. 12 (2) (2018) 026011, , https://doi.org/10.1117/1.JRS.12.026011.
[22] F. Pirotti, C. Zanchetta, M. Previtali, S. Della Torre, Detection of building roofs and facades from aerial laser scanning data using deep learning, ISPRS-International Archives of the Photogrammetry, Remote Sensing and Spatial Information Sciences 4211 (2019) 975–980, https://doi.org/10.5194/isprs-archives-XLII-2-W11-975-2019.
[23] INSPIRE Geoportal, http://inspire-geoportal.ec.europa.eu/ (Last access: 27/03/2019).
[24] Downloading Centre – Spanish Centre of Geographic Information, http://centrodedescargas.cnig.es/CentroDescargas/index.jsp (Last access: 27/03/2019).
[25] A. Sampath, J. Shan, Building boundary tracing and regularization from airborne LiDAR point clouds, Photogramm. Eng. Remote Sens. (7) (2007) 805–812, https://doi.org/10.14358/PERS.73.7.805.
[26] G.M. Gandhi, S. Parthiban, N. Thummalu, A. Christy, NDVI: vegetation change detection using remote sensing and GIS – a case study of Vellore District, Proc. Comput. Sci. 57 (2015) 1199–1210, https://doi.org/10.1016/j.procs.2015.07.415.
[27] A.K. Bhandari, A. Kumar, G.K. Singh, Feature extraction using Normalized Difference Vegetation Index (NDVI): a case study of Jabalpur City, Proc. Technol. 6 (2012) 612–621, https://doi.org/10.1016/j.protcy.2012.10.074.
[28] K. Jordan, P. Mordohai, A quantitative evaluation of surface normal estimation in point clouds, 2014 IEEE/RSJ International Conference on Intelligent Robots and Systems, IEEE, 2014, , https://doi.org/10.1109/IROS.2014.6943157.
[29] Point Cloud Library (PCL) Documentation, http://pointclouds.org/documentation/tutorials/statistical_outlier.php#statistical-outlier-removal (Last access: 27/03/2019).
[30] The Spanish Technical Building Code (Royal Decree 314/2006 of 17 March 2006), Available online https://www.codigotecnico.org/ (Last access: 27/03/2019).
[31] A. Nurunnabi, G. West, D. Belton, Outlier detection and robust normal-curvature estimation in mobile laser scanning 3D point cloud data, Pattern Recogn. 48 (4) (2015) 1404–1419, https://doi.org/10.1016/j.patcog.2014.10.014.
[32] R. Nock, F. Nielsen, Statistical region merging, IEEE Trans. Pattern Anal. Mach. Intell. 26 (11) (2004) 1452–1458, https://doi.org/10.1109/TPAMI.2004.110.
[33] R.G. Von Gioi, J. Jakubowicz, J.M. Morel, G. Randall, LSD: a line segment detector, Image Process. On Line 2 (2012) 35–55, https://doi.org/10.5201/ipol.2012.gjmr-lsd.
[34] R.G. Von Gioi, J. Jakubowicz, J. Morel, G. Randall, LSD: a fast line segment detector with a false detection control, IEEE Trans. Pattern Anal. Mach. Intell. 32 (4) (2010) 722–732, https://doi.org/10.1109/TPAMI.2008.300.
[35] M.A. Fischler, R.C. Bolles, Random sample consensus: a paradigm for model fitting with applications to image analysis and automated cartography, Commun. ACM 24 (6) (1981) 381–395, https://doi.org/10.1145/358669.358692.
[36] F. Rottensteiner, G. Sohn, M. Gerke, J.D. Wegner, ISPRS test project on urban classification and 3D building reconstruction, Commission III-Photogrammetric Computer Vision and Image Analysis, Working Group III/4-3D Scene Analysis, 2013, pp. 1–17 http://www.cvlibs.net/projects/autonomous_vision_survey/literature/Rottensteiner2013.pdf (Last access: 21/10/2019).
[37] S. Roberts, N. Guariento, Building Integrated Photovoltaics: A Handbook, Birkhäuser, Basel, 978-3764399481, 2009, https://doi.org/10.1007/978-3-0346-0486-4.
[38] G. Gaussorgues, S. Chomet, Infrared Thermography, vol. 5, Springer Science & Business Media, 978-0470682234, 2012, https://doi.org/10.1002/9780470682234.